

A non cool-core 4.6-keV cluster around the bright nearby radio galaxy PKS B1416–493

D.M. Worrall and M. Birkinshaw

HH Wills Physics Laboratory, University of Bristol, Tyndall Avenue, Bristol BS8 1TL

3 February 2017

ABSTRACT

We present new X-ray (*Chandra*) and radio (*ATCA*) observations of the $z = 0.09$ radio galaxy PKS B1416–493, a member of the southern equivalent of the 3CRR sample. We find the source to be embedded in a previously unrecognized bright $kT = 4.6$ -keV non cool-core cluster. The discovery of new clusters of such high temperature and luminosity within $z = 0.1$ is rare. The radio source was chosen for observation based on its intermediate FRI/II morphology. We identify a cavity coincident with the northeast lobe, and excess counts associated with the southwest lobe that we interpret as inverse Compton X-ray emission. The jet power, at 5.3×10^{44} erg s^{−1}, when weighted by radio source density, supports suggestions that radio sources of intermediate morphology and radio power may dominate radio-galaxy heating in the local Universe.

Key words: galaxies: active – galaxies: clusters: general – galaxies: individual: (PKS B1416–493) – galaxies: jets – radio continuum: galaxies – X-rays: galaxies: clusters

1 INTRODUCTION

The last two decades have seen increasing awareness that radio jets are efficient conveyors of momentum flux and AGN energy to large distances: simulations show the need for such an extra heat source on cosmological scales (see review by Somerville & Davé 2015), and *Chandra* and *XMM-Newton* have provided spectacular demonstrations of radio galaxy/gas interactions in individual sources (reviewed by McNamara & Nulsen 2007; Fabian 2012).

Observations have found many X-ray gas cavities bored by radio lobes, and often the energy expended, scaled by AGN duty cycle, appears sufficient to replenish that lost to radiative cooling (e.g., Birzan et al. 2004; Dunn, Fabian & Taylor 2005; Panagoulia et al. 2014). How the energy is dispersed, if favorable heating and cooling feedback cycles are to be established, is more uncertain. The most widely discussed ideas tend to involve the buoyant rise of gas cavities, subsonic inflation, and sound waves (see review by McNamara & Nulsen 2012).

Radio sources at redshift $z < 0.1$ can be studied with high linear resolution and are the best-suited for investigating the interactions between the relativistic jet plasma and the external (X-ray-emitting) medium. Of these, low-power sources of the FRI class are the most numerous and widely studied. Detection of X-ray synchrotron emission from their jets has become common with *Chandra* (Worrall et al. 2001)

(and see review by Worrall 2009). The mechanical power of the radio source can be estimated through its work on the X-ray gas by combining the enthalpy of lobe cavities with cavity age (Birzan et al. 2004). The values found are used as a proxy for total jet power, P_{jet} . While P_{jet} dominates the power in radiation-mediated channels, it has nevertheless been found to correlate with radiative power, P_{rad} (Birzan et al. 2008), with the latest work suggesting slopes at the steeper extreme of earlier values: P_{jet} roughly proportional to $P_{\text{rad}}^{0.7}$ (Cavagnolo et al. 2010; O’Sullivan et al. 2011). Godfrey & Shabala (2016) have argued that since the correlations plot power on both axes, common distance spreading, forcing correlations to slopes approaching unity, may be a strong factor driving the results. However, the main sample on which the correlation is founded uses radio observations to whatever depth is needed to match observed X-ray cavities, and so should be unbiased (P. Nulsen 2016, private communication). In any case, as new radio-source cavities are discovered they can be tested against the claimed jet-power/radiative-power correlation, and, pushing to sources of somewhat higher power, the steeper correlation (albeit with its broad dispersion) seems to be holding up (e.g., Croston et al. 2011; Worrall et al. 2012). Earlier wisdom had been that strong shocks are not important in the dynamics and heat deposition of radio sources (McNamara & Nulsen 2007), and it is noteworthy that this

situation has been seen to change at somewhat higher radio powers, where the work done in driving shocks dominates cavity power alone, for example in both 3C 444 and PKS B2152–699 (Croston et al. 2011; Worrall et al. 2012).

When radio power is weighted by source density the correlation between jet power and radio power implies that radio sources lying close to the break in the radio luminosity function (e.g., Best et al. 2005) should provide the greatest contribution of jet power in the local Universe. Indeed, we estimate that half of the total jet-power output should be from sources with radio powers within a factor of three of $3 \times 10^{25} \text{ W Hz}^{-1}$ at 1.4 GHz (i.e., $L_{1.4 \text{ GHz}}$ between 1.4 and $12.6 \times 10^{41} \text{ erg s}^{-1}$). Such sources typically show morphologies intermediate between FRI and FRII, and for our present purposes we define sources within this power range to be FRI/II boundary sources. It is of particular interest to study the environments and jet-gas interactions of these sources because of their inferred disproportionately large contribution to feedback.

The 3CRR catalogue contains the brightest radio sources in the northern sky, and within it there are 16 FRI/II boundary sources at $z < 0.1$, all observed with *Chandra* and some also with *XMM-Newton*. The complete subsample (Birkinshaw et al. in preparation) contains two broad-line radio galaxies where the X-ray emission is dominated by the core, and several cases where the hot-gas environment appears to have expanded away. Notable low-redshift 3CRR FRI/II boundary sources where jet-gas interactions are reported are 3C 35 (Mannering, Worrall & Birkinshaw 2013), 3C 192 (Hodges-Kluck et al. 2010), 3C 285 (Hardcastle et al. 2007), 3C 305 (Hardcastle et al. 2012), 3C 310 (Kraft et al. 2012), and 3C 465 (Hardcastle, Sakellou & Worrall 2005). Of these both 3C 305 and 3C 310 have prominent atmospheres and exhibit strong shocks: a shock with Mach number $\mathcal{M} \approx 1.7$ is seen in 3-keV gas around 3C 310, and in the smaller-scale and cooler ($kT \approx 0.4 \text{ keV}$) gas around 3C 305, $\mathcal{M} \approx 2$ is inferred.

To extend the number of FRI/II boundary sources for which heating mechanisms can be studied we have turned to the southern hemisphere. The MS4 catalog is the southern equivalent of 3CRR (Burgess 1998; Burgess & Hunstead 2006a,b). Our joint *Chandra* and *ATCA* programme concentrated first on the brightest FRI/II boundary source in the catalogue, the $z = 0.0282$ radio galaxy PKS B2152–699 (Worrall et al. 2012). Here we found X-ray cavities, lobe-inverse Compton emission, an atmosphere of $kT \approx 1 \text{ keV}$, intermediate between those of 3C 305 and 3C 310, and strong shocks bounding the lobes with \mathcal{M} in the range 2.2 to 3. PKS B2152–699 is of further interest in exhibiting a localized jet-gas interaction region first reported in the form of a High Ionization Cloud (HIC) (Tadhunter et al. 1987) adjacent to the jet, and now known to be associated with both a significant X-ray-emitting atmosphere and jet bending (Worrall et al. 2012). A similar interaction is also now known for 3C 277.3 (Worrall, Birkinshaw & Young 2016). PKS B2152–699 has rounded radio lobes but with hotspots that are embedded rather than at the extremities, a common feature of FRI/II boundary objects (Capetti, Fanti & Parma 1995). Its nuclear optical spectrum is of intermediate ionization and exhibits both forbidden and permitted lines with broad wings (Tadhunter et al. 1988),

and so it would be classed as a high excitation radio galaxy (HERG).

In this paper we report the X-ray (*Chandra*) and radio (*ATCA*) properties of a second MS4-catalogue FRI/II boundary source, PKS B1416–493. The 4.8-GHz radio map of Burgess (1998) already showed evidence for embedded hotspots. PKS B1416–493 has other radio similarities to PKS B2152–699. If moved from its redshift of $z = 0.0914$ (Jones et al. 2009) to that of PKS B2152–699, its 408-MHz flux density would be 76.7 Jy, as compared with 61.6 Jy for PKS B2152–699. Its angular extent would be 128 arcsec, as compared with 80 arcsec for PKS B2152–699. Its 1.4-GHz core flux density would be 529 mJy, as compared with 770 mJy for PKS B2152–699. There is a difference: in contrast to PKS B2152–699 the nuclear optical emission of PKS B1416–493 shows only weak H_α and [NII] (Simpson et al. 1996), and it would be classed as a low excitation radio galaxy (LERG).

X-ray emission associated with PKS B1416–493 was first reported with *ROSAT*: the source appears in the Bright Source Catalog as 1RXS J142001.8–493554 (Voges et al. 1999), and subsequently it is listed in the 3–20-keV *RXTE* all-sky slew survey (Revnivtsev et al. 2004). The source has attracted little attention, perhaps because it is in the Southern sky at a Galactic latitude of only 10.8 degrees and at –43 degrees Galactic longitude. It was not previously identified as a cluster of galaxies, nor are there reports of a cluster based on optical observations of the galaxy field.

In this paper we report the properties of the cluster, and the jet-gas interactions and energetics. We adopt values for the cosmological parameters of $H_0 = 70 \text{ km s}^{-1} \text{ Mpc}^{-1}$, $\Omega_{m0} = 0.3$, and $\Omega_{\Lambda 0} = 0.7$. Thus 1 arcsec corresponds to a projected distance of 1.7 kpc at PKS B1416–493.

Throughout the paper the power-law spectral index, α , is defined in the sense that flux density is proportional to $\nu^{-\alpha}$. X-ray spectral indices are quoted in terms of α rather than the values one larger returned by spectral-fitting codes. Uncertainties correspond to 90 per cent confidence for the parameter of interest, unless otherwise stated.

2 OBSERVATIONS AND REDUCTION METHODS

2.1 *Chandra* X-ray

Our observations of PKS B1416–493 were with the *Chandra* Advanced CCD Imaging Spectrometer (ACIS) in VFaint full-frame data mode on 2015 June 3rd (OBSID 17058). The source was positioned at the nominal aimpoint of the I3 chip, and the three other ACIS-I chips and the ACIS-S S2 chip also received data (see the *Chandra* Proposers’ Observatory Guide¹ for details of the instrument and its modes). We followed the software ‘threads’ from the *Chandra* X-ray Center (CXC)² to re-calibrate the data with the energy-dependent sub-pixel event repositioning algorithm applied. Results presented here use CIAO V4.8 and the CALDB V4.7.2 calibration database.

The observations were free from background flares and,

¹ <http://cxc.harvard.edu/proposer>

² <http://cxc.harvard.edu/ciao>

Table 1. ATCA radio data in programme C2936

(1) Frequency (GHz)	(2) On-source time (h)	(3) Restoring Beam (arcsec) ²	(4) Stokes I noise (μ Jy beam ⁻¹)
5.5	2.3	1.99×1.17	26
9.0	2.3	1.29×0.70	21
18.0	4.5	0.50×0.50	17

after removal of time intervals when the background deviated more than 3σ from the average value, the exposure time was 62.829 ks. We adjusted the astrometry by 0.36 arcsec, mostly in RA, to align the X-ray nucleus with the radio core position measured to be RA = $14^{\text{h}}20^{\text{m}}03^{\text{s}}.704$, Dec = $-49^{\circ}35'42''.06$ (see Section 2.2).

The CIAO WAVDETECT task was used to find sources in the 0.4–5-keV image, with the threshold set at 1 spurious source per field. Except for those detections corresponding to features associated specifically with features of PKS B1416–493, the corresponding regions were masked and corrected for in quantitative analyses. All spectral models include absorption along the line of sight in our Galaxy with a column density of $N_{\text{H}} = 1.49 \times 10^{21} \text{ cm}^{-2}$, as given by the CXC COLDEN task using data of Dickey & Lockman (1990). Spectral fitting uses XSPEC³ version 12.9.0u with the abundance table of Anders & Grevesse (1989).

For analysis where we sample the background using blank-sky fields, in contrast to using a local off-source measure of the background, we followed procedures described in the CXC software threads. We cleaned the source and sky-background data using the same criteria, and re-projected the background data to the coordinate system of the source. A small downwards correction factor of 3.5% was applied to the background rates so that the on-source and background rates match at 9.5–12-keV where the particle component of the background dominates.

2.2 ATCA radio

We observed PKS B1416–493 with the ATCA in its 6B array configuration with the Compact Array Broadband Backend (CABB) correlator (Wilson et al. 2011) on 2014 August 26th (programme C2936). Data were taken in 2048 1-MHz wide channels centred at either 17 and 19 GHz or 5.5 and 9 GHz. The planned observing schedule was modified to take account of the wet and thundery weather conditions, so that less time was spent at the higher frequencies than planned, and additional calibration was performed. Some time was lost to periods of high wind or local lightning. A summary of the on-source time achieved is given in Table 1, which also shows the restoring beams and noise levels of the three maps made, centred at 5.5, 9, and 18 GHz.

Sources B1921–293 and B1934–638 were observed for bandpass and primary flux calibration, respectively. B1421–490, a small-angular size source near PKS B1416–493, was observed for phase calibration and as a pointing and focus reference. Data calibration was carried

out with the MIRIAD⁴ software using the calibration advice for CABB data given in the 2010 September version of the Miriad User Guide, with the central 90% of each 2-GHz band being used for mapping.

Extensive data flagging was required before and after calibration to remove interference (at 5.5 or 9 GHz) and periods when the atmosphere was highly unstable. At 5.5 and 9 GHz multi-frequency synthesis using the entire band was successful at generating useful images, via the normal self-calibration cycle. The 18-GHz map, created from the 17-GHz and 19-GHz data, could not be made in this way because significant time-dependent phase slopes were seen across the bandpass, presumably from atmospheric delays. An approximate correction for this was done by dividing each of these two bands into eight sub-bands in frequency, and then self-calibrating each sub-band separately against the multi-frequency synthesis map. Large amplitude changes from uncorrected atmospheric opacity changes were also removed in this procedure.

The noise levels in the final Stokes I maps are affected by residual phase and amplitude errors, but these are negligible at the contour levels presented here, and dynamic ranges of about 10^3 are achieved over much of the area of the images. Polarization images were also made, and show significant features in bright parts of the radio emission, though only a trace of polarization associated with the inner part of the jet can be seen near the core.

3 RESULTS AND DISCUSSION

3.1 The radio galaxy

Our new radio mapping confirms the structure of PKS B1416–493 (Fig. 1) to be of intermediate FRI/II morphology. It displays two radio lobes NE and SW of the radio core, with a jet connecting the core to the brightest part of the SW lobe, and a faint bridge connecting the lobes. At low surface-brightness levels both lobes appear approximately circular, but while the bright region in the smaller NE lobe is placed centrally, that in the SW lobe, which lies at approximately the same distance from the core as in the NE lobe, is displaced away from the centre of the lobe.

A prominent flat-spectrum jet knot (Table 2), of 1 arcsec angular extent, lies about 3 arcsec SW of the core, and is connected to it, and to the brightest structure in the SW radio lobe, by fainter emission. The jet from the core to the bright knot is misaligned with the line from the core to the brightest compact component in the SW lobe: the radio knot appears to mark a kink in the jet. Polarization data suggest that the magnetic field changes direction from parallel to perpendicular to the jet axis at this kink. Beyond the knot the jet bends again, and appears to terminate at an interior hot spot at RA = $14^{\text{h}}20^{\text{m}}02^{\text{s}}.48$, Dec = $-49^{\circ}35'50''.7$ in the SW lobe. This hot spot lies at the end of a bright curved ridge which extends to the E, with the apparent magnetic field running parallel to the ridge.

No such well-defined structure is seen in the NE lobe, though a fainter, possibly compact, component lies diametrically opposite the hot spot seen in the SW lobe, at the

³ <https://heasarc.gsfc.nasa.gov/xanadu/xspec/>

⁴ <http://www.atnf.csiro.au/computing/software/miriad>

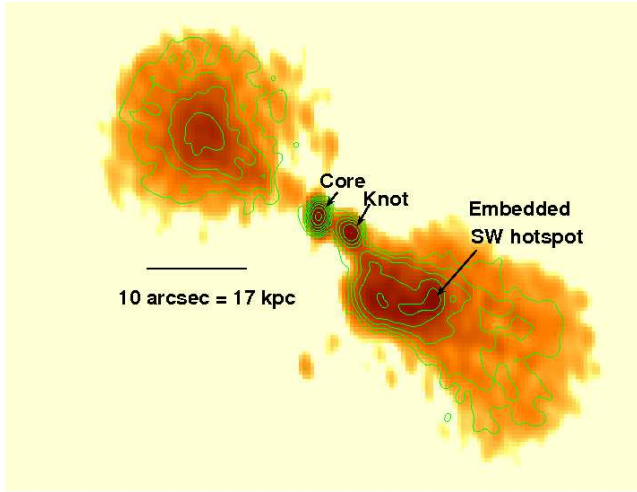


Figure 1. The 5.5 GHz radio map overlaid with contours from the 9-GHz map (Table 1) showing the overall structure of the radio galaxy. The contours increase by factors of 2 from a lowest level of $0.2 \text{ mJy beam}^{-1}$.

Table 2. Radio components

(1) Component	(2) $S_{5.5 \text{ GHz}}$ (mJy)	(3) $S_{9 \text{ GHz}}$ (mJy)	(4) $S_{18 \text{ GHz}}$ (mJy)	(5) α	(6) Notes
Core	56 ± 3	56 ± 1	75 ± 4	0.00	
Jet knot	26 ± 2	16 ± 1	12 ± 1	0.42	a,c
NE lobe	221 ± 5	133 ± 3	48 ± 3	1.03	b,d
SW lobe	324 ± 7	196 ± 4	93 ± 5	1.02	b,e

Flux densities include systematic flux scale errors of 2% at 5.5 and 9 GHz, and 5% at 18 GHz because of poor weather during the observations.

a. Jet knot spectrum taken from 9 to 18 GHz: 5-GHz flux density confused with inner lobe.

b. Lobe spectrum taken from 5.5 to 9 GHz: at 18 GHz the lobe is over-resolved, and the flux density in the table relates only to the compact inner region.

c. Knot angular size (Gaussian deconvolved FWHM) 1.1×0.2 arcsec.

d. NE lobe diameter about 22 arcsec, but the brightest region has a diameter of about 8 arcsec.

e. SW lobe diameter about 27 arcsec, but the brightest region has a diameter of about 12 arcsec.

same distance from the core. The bright region in the NE lobe is fainter than that in the south, and is relatively poorly represented in the present data because of the poor weather during the observation.

The radio core is essentially unpolarized and of flat radio spectrum from 5.5 to 9 GHz, but then brightens to 18 GHz, suggesting the presence of a small-scale self-absorbed component. A faint polarized extension of the core to the SW seen on our highest-resolution 18-GHz map can be interpreted as the base of the kpc-scale jet.

An unrelated point source lies at the edge of the SW lobe, at RA = $14^{\text{h}}20^{\text{m}}03^{\text{s}}.84$, Dec = $-49^{\circ}35'57''.4$.

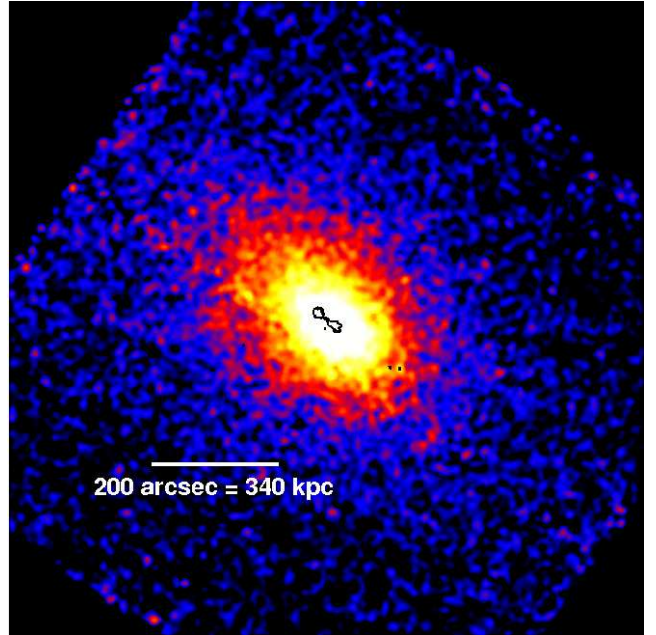


Figure 2. 0.4-5-keV exposure corrected *Chandra* image showing the lie of the cluster on the four ACIS-I chips. The image is in native 0.492-arcsec pixels and smoothed with a Gaussian of standard deviation $\sigma = 10$ pixels. Point sources have been removed. The lowest contour from Figure 1 (black) shows that the radio source lies central to the cluster.

3.2 Large-scale X-ray emission

From an exposure-corrected image, X-ray emission reminiscent of cluster emission in excess of background is visually apparent over a large fraction of ACIS-I (Fig. 2). The $R = 15.7$ mag host galaxy of PKS B1416–493 (Jones et al. 2009) can be identified as the central brightest cluster galaxy (BCG), and we see that the radio extent is quite well aligned in projection with the major axis of the cluster emission.

For an initial exploration of the cluster properties, the spectrum of the brightest part of the extended X-ray emission was measured from an elliptical region of semi-major and semi-minor axes 52.7 and 34.3 arcsec, respectively, centered on the position of the radio core. This on-source region lies entirely on the I3 chip, and background was sampled from a more remote part of the same chip, to the north of the brightest cluster emission. The spectrum fits well a single-temperature thermal (APEC) model ($\chi^2 = 172.9$ for 152 degrees of freedom) with $kT = 4.72^{+0.36}_{-0.35}$ keV and abundances relative to Solar of $0.54^{+0.17}_{-0.15} Z_{\odot}$. This indicates a relatively rich cluster, not previously catalogued. Similar spectral results were obtained using background from a matched region on the blank-sky fields, processed as described in Section 2.1.

Our in depth characterisation of the cluster emission uses exclusively blank-field background subtraction. For ease of measurement, and because we do not know the extent of the cluster emission along the line of sight, we have used a spherical approximation to model the large-scale gas distribution. Figure 3 shows the 0.5–7-keV exposure-corrected radial profile, centered on the radio core, fitted to a β model. The quality of fit is excellent. Temperature and abundance profiles, constructed to provide roughly 2500 net counts in each bin, are shown in Figure 4. The quality of the individ-

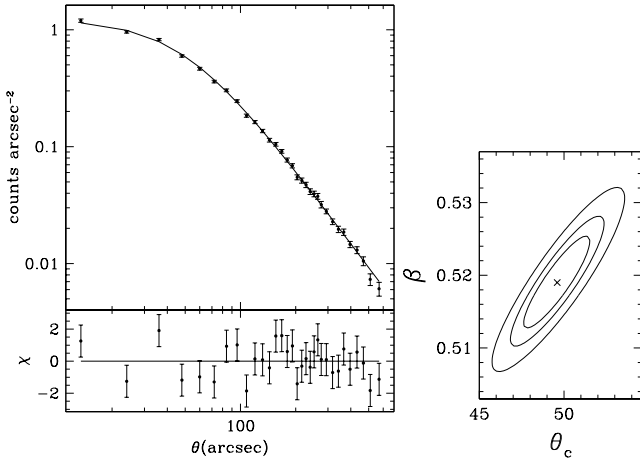


Figure 3. *Left:* Background-subtracted exposure-corrected 0.5–7-keV radial profile fitted to a β -model profile with the residuals (shown as a contribution to χ) in the lower panel. The best fit is for a core radius of $\theta_c = 49.6$ arcsec and $\beta = 0.519$ ($\chi^2/\text{dof} = 33.7/29$). *Right:* Uncertainty contours (1σ , 90% and 99% for 2 interesting parameters) of θ_c and β for the radial-profile fit.

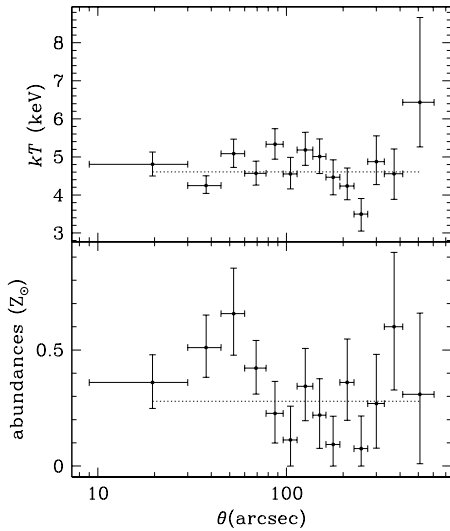


Figure 4. *Chandra* X-ray projected temperature and abundance profiles of the cluster showing consistency with uniformity. Individual errors are 1σ for one interesting parameter. Upper panel shows kT : average value is 4.61 keV, $\chi^2/\text{dof} = 19.3/13$. Lower panel shows abundances: average value is $0.28 Z_\odot$, $\chi^2/\text{dof} = 19.2/13$.

ual spectral fits is acceptable at better than 95% confidence. Any deviations from uniformity are small and not highly significant, and we find average values of kT and abundance in annuli out to 10 arcmin of 4.6 keV and $0.28 Z_\odot$, respectively. In particular, there is no evidence for a cluster-scale large cool core.

For the cluster’s measured temperature, the scaling relations of Vikhlinin et al. (2006) give a value of r_{500} of 617 arcsec (1.053 Mpc), which is also approximately the distance to which these observations detect the cluster. Properties of the cluster are summarized in Table 3. The values have been measured using the radial profile (Fig. 3) and average spectral properties (Fig. 4) using equations given

Table 3. Cluster Properties

(1) Parameter	(2) Value
β	0.519 ± 0.009
core radius, r_c	84.7 ± 4.4 kpc
FWHM	163 ± 5 kpc
Average kT	4.61 ± 0.17 keV
Average abundances	$0.28 \pm 0.04 Z_\odot$
Bolometric $L_{r_{500}}$	$(2.73 \pm 0.02) \times 10^{44}$ erg s $^{-1}$
Central gas density	$(5.5 \pm 0.2) \times 10^3$ m $^{-3}$
Central pressure	$(9.3 \pm 0.4) \times 10^{-12}$ Pa
Central cooling time	$(1.00 \pm 0.05) \times 10^{10}$ yr
Mass deposition rate within r_c	$23.5 \pm 1.7 M_\odot$ yr $^{-1}$
Gas mass within r_{500}	$(4.05 \pm 0.25) \times 10^{13} M_\odot$
Total mass within r_{500}	$(2.79 \pm 0.12) \times 10^{14} M_\odot$

Errors are statistical only. Unknown geometry contributes additional uncertainties.

in Birkinshaw & Worrall (1993) and Worrall & Birkinshaw (2006).

We conclude that PKS B1416–493 lies in an extreme atmosphere amongst the studied FRI/II boundary objects. Perhaps the closest examples in 3CRR are 3C 388 and 3C 338, both classified as LERGS. 3C 388 falls just beyond our definition of a FRI/II boundary object in the direction of high radio power, and has been found to reside in a $kT \approx 3.5$ keV cluster with no strong cool core (Kraft et al. 2006). PKS B1416–493 is more extreme in having a richer X-ray atmosphere and longer central cooling time. 3C 338 falls just beyond our definition of a FRI/II boundary object in the direction of low radio power. It lies within the cool core of the $kT \approx 4.5$ keV cluster Abell 2199, and both radio source and cluster are highly disturbed as a result of merger activity (Nulsen et al. 2013).

Ineson et al. (2015) finds a correlation between radio power and the X-ray luminosity of the environment for radio galaxies classed as LERGS. The correlation is driven by a shortage of lower-power sources in rich clusters and higher-power sources in weak atmospheres, and in a broadened intermediate FRI/II boundary region the atmospheres span three orders of magnitude in X-ray luminosity. PKS B1416–493 is perhaps remarkable less in the richness of its X-ray-emitting atmosphere than in that atmosphere having been unrecognized before now.

3.3 Cluster ellipticity and AGN location

In an attempt to characterise the ellipticity of the cluster we first applied the IRAF STSDAS ELLIPSE software⁵ to the smoothed data of Figure 2. This provided representations of the ellipticity and position angle of the cluster emission on scales larger than the radio source that were used to set starting values in subsequent fitting using the CIAO SHERPA package. For SHERPA we binned the exposure-corrected 0.4–5 keV image into 2-arcsec pixels, fitted over a large region of roughly 9 by 11.5 arcmin oriented with the cluster, and used the cstat statistic because most bins contained few counts.

⁵ http://www.stsci.edu/institute/software_hardware/stsdas

On top of a flat background of fitted amplitude, an elliptical Gaussian represented the cluster gas, and its parameters were allowed to be free. A small-scale elliptical Gaussian was used as a crude representation of the combined core and galaxy emission, discussed later in more detail in Sections 3.4 and 3.6, and a circular Gaussian of fixed position and 1.5 arcsec FWHM was used to represent the knot emission discussed later in Section 3.7. The overall fit was acceptable, as given by the cstat criterion that the fit statistic divided by the number of degrees of freedom should be approximately one.

Figure 5 shows the residual between data and model for the inner regions. Spatially-correlated residuals show that the true structure is more complex than the model used. In particular, there are correlated negatives underlying the NE radio lobe, whereas residuals in the SW have a greater tendency to be positive. The central regions are generally poorly represented, with what appears to be an excess to the NW of the radio knot that extends in a line to the E of the SW radio lobe, and an excess bounding the inner edge of the NW lobe. These emissions are apparent in the original image and, while they may represent disturbed gas, a much deeper X-ray observation would be required to investigate morphology and origin. We note that SHERPA fitting is restricted to conformal ellipses, whereas visual examination and our ELLIPSE fitting suggest that the cluster is more complex in spatial structure with ellipticity, position angle, and centre varying with radius.

The elliptical component describing the cluster in the SHERPA fit is found to be centered at $RA = 14^h 20^m 03^s.45 \pm 0.04$, $Dec = -49^\circ 35' 43''.6 \pm 0.6$. The radio core is 2.9 arcsec (4.9 kpc) to the NE of this, and so even without considering the third dimension, the BCG is not located precisely at the cluster centre and relative motion is expected. This is also suggested by the radio structure, where the pronounced NE-SW asymmetry is consistent with motion in a projected NE direction. Ram pressure would then explain the rounding of the more compact NE lobe, whereas instabilities of flow along the side of the trailing SW lobe would contribute to its outer plume-like appearance.

3.4 Galaxy atmosphere

To investigate the X-ray emission from the host galaxy of PKS B1416–493 we extended the radial profile of Figure 3 into the core, masking a region around the knot and truncating the cluster emission at $126''$. In fitting the radial profile we fixed the values of β and core radius representing cluster gas to values found in Section 3.2. To represent the core we simulated and merged 50 representations of the point spread function (PSF) using the CXC SAOSAC RAYTRACE and MARX software for the spectral model described in Section 3.6, and included this with free amplitude. We modelled the galaxy emission as a second β -model, but since it is of small scale it was convolved with the PSF. The best overall model fit, shown in Figure 6, is formally marginally acceptable, and we take it as including a reasonable representation of galaxy-related emission in the central region. A deeper X-ray observation would be required to warrant more complex modelling, which could then allow for small offsets between cluster centre and AGN core, as discussed in Section 3.3.

Guided by Figure 6, spectral fitting of the galaxy-

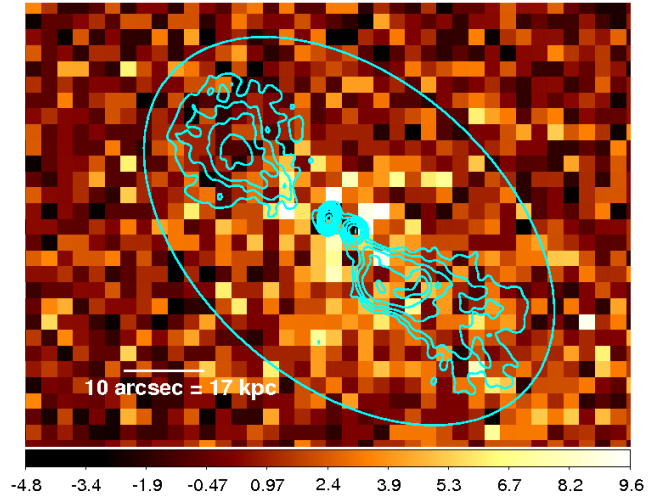


Figure 5. Residual 0.4–5 keV exposure-corrected *Chandra* image in 2-arcsec pixels from a simple model with small elliptical and circular components at the core and knot, respectively, and a large elliptical component representing the cluster gas. Colour scale is in units of counts. Overlaid are the radio contours as in Figure 1, and an isophote of the cluster model to indicate its orientation and ellipticity. The residuals show an asymmetry, with negative values under the NE lobe and positive values across the centre and in the SW.

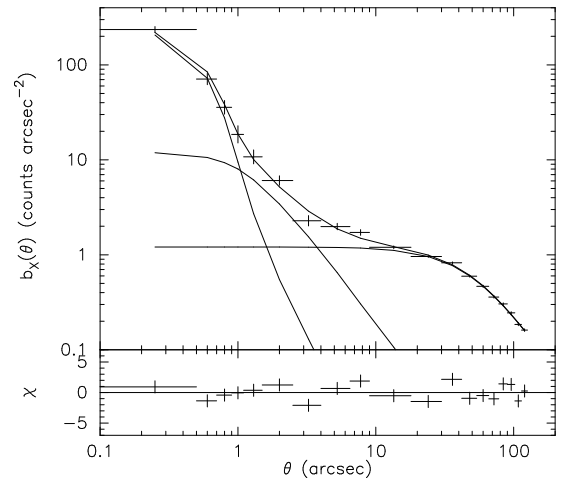


Figure 6. As Fig. 3 but reaching in to the AGN. The broadest model component has been fixed to the best-fit cluster values. The other two model components are the PSF, representing the AGN core, and a β -model convolved with the PSF, representing galaxy-scale gas. The best fit finds $\beta = 0.49$, $\theta_c = 0.97$ arcsec ($\chi^2/\text{dof} = 27.9/16$).

scale emission was performed by extracting counts from a core-centred annulus of radii 1.3 and 5 arcsec, with background from a core-centred annulus of radii 9 and 12 arcsec. There were too few counts to attempt models more complex than a simple single-temperature thermal model, and whereas cluster emission should be accounted for by the choice of background region, contamination from the core PSF and emission from X-ray binaries in the host galaxy of PKS B1416–493 is not. We found an adequate fit to $kT = 1.6^{+1.8}_{-0.8}$ keV ($\chi^2/\text{dof} = 6.7/8$). The best-fit abundance

Table 4. Galaxy gas properties

(1) Parameter	(2) Value
β	0.5 ± 0.1
core radius, r_c	$1.7^{+1.7}_{-1.2}$ kpc
FWHM	3.2^{+3}_{-2} kpc
Average kT	$1.6^{+1.8}_{-0.8}$ keV
$L_{0.5-2 \text{ keV}} (< 5'')$	$(4.5 \pm 1.0) \times 10^{41} \text{ erg s}^{-1}$
Gas density at $5''$	$(15 \pm 2) \times 10^3 \text{ m}^{-3}$
Cooling time at $5''$	$(2^{+1}_{-0.7}) \times 10^9 \text{ yr}$
Mass deposition rate within r_c	$0.4^{+0.4}_{-0.3} \text{ M}_\odot \text{ yr}^{-1}$
Gas mass within $5''$	$(1.0^{+2.5}_{-0.9}) \times 10^{10} \text{ M}_\odot$

Errors are statistical only.

is $0.3 Z_\odot$, but with unconstrained errors. We have used the temperature together with the fitted spatial parameters of the radial profile to derive properties of the galaxy gas given in Table 4.

The galaxy atmosphere is not unusual for the host of a radio galaxy — even with *ROSAT* the techniques we have used here could separate thermal atmospheres of galaxy scale from central AGN in the closest radio galaxies (Worrall & Birkinshaw 1994), and work has been extended to many more sources using the much narrower PSF of *Chandra*. Sun (2009) refers to galaxy-scale atmospheres as coronae, distinguishing them from cluster cool cores of the type absent around PKS B1416–493, further suggesting that the radio outbursts made possible by the presence of coronae in turn help destroy embryonic cluster cool cores. Radial profiles of cool-core clusters (e.g., Henning et al. 2009) lack the flattening and inflection between cluster and galaxy core radii seen in PKS B1416–493 (Fig. 6).

3.5 Lobes and jet power

Figure 7 presents radio contours on a smoothed image of the X-ray emission. The more rounded NE lobe appears to lie against a deficit of X-ray emission as compared with the SW lobe. We have quantified this by sampling background for each lobe from regions in sectors 90° away and extending over similar cluster-modelled elliptical annuli. The NE lobe shows no excess relative to the cluster at a 90%-confidence upper limit of 0.9 nJy at 1 keV (adopting a power-law spectrum of index consistent with the radio). In the case of the SW lobe the excess (about 15% of the surrounding cluster surface brightness) gives a good fit to a power-law spectrum of $\alpha_x = 1.2^{+1.9}_{-1.1}$ ($\chi^2/\text{dof} = 6.7/9$) with a 1-keV flux density of $4.8^{+4.9}_{-3.3}$ nJy. The fit to a thermal model is equally good with $kT = 3.3^{+2.2}_{-2.2}$ ($\chi^2/\text{dof} = 6.5/9$).

It is attractive to interpret the X-ray excess in the SW lobe as due to inverse Compton scattering by the radio synchrotron-emitting electron population, as supported by the agreement of radio and X-ray spectral indices. Pressure arguments back this up. Firstly, we have used the radio data in Table 1 to calculate the total pressures for an equipartition magnetic field in each lobe, following Hardcastle, Birkinshaw & Worrall (1998), and have compared with gas pressures at similar projected distances from the core measured through our X-ray radial-profile and spec-

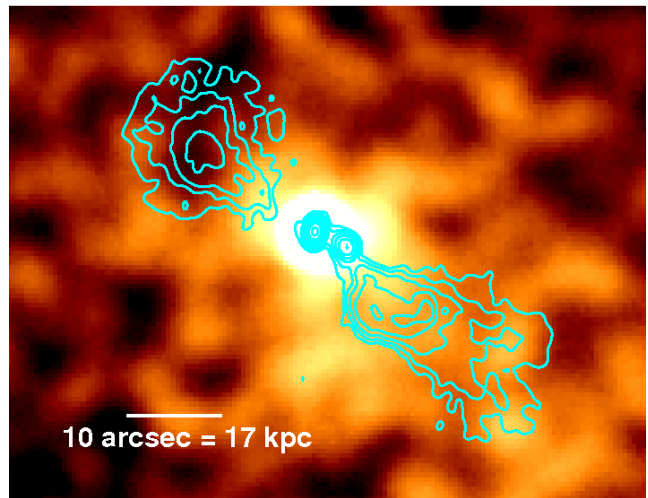


Figure 7. Contours of the 9-GHz radio map, as in Figure 1, superimposed on a 0.4–5 keV exposure-corrected *Chandra* image in native 0.492-arcsec pixels, where data have been smoothed with a Gaussian of $\sigma = 4$ pixels. There is a deficit of X-ray emission projected onto the NE lobe as compared with the SW.

tral fitting (Table 5). We find lobe underpressure by a factor of eight (columns 3 and 4, Table 5), which can be restored to balance by increasing or decreasing lobe field strength to the values shown in column 5, or by adding protons. For the SW lobe, decreasing the field strength to a factor of four below equipartition gives both an excellent match to the gas pressure and an inverse-Compton prediction that matches the X-ray excess (Fig. 8). It is of course likely that the lobe is overpressured and the external gas shocked, as can be achieved by adding a likely component of relativistic protons. Shocked gas is very difficult to see in hot clusters like this one, although such gas is measured at a Mach number of roughly 3 in the 1-keV atmosphere around PKS B2152–699 (Worrall et al. 2012). There is no evidence for PKS B1416–493 being at small angle, θ , to the line of sight, but if, for example, $\theta = 30^\circ$, the inverse-Compton required field of 0.5 nT would leave the SW lobe overpressured by only a factor of 1.3, although this is before consideration of a proton contribution.

It seems reasonable that departures from equipartition would not be too dissimilar between opposing radio lobes, and departures in the sense of magnetic fields being lower by factors of around three are rather common for radio-galaxy lobes in general (Croston et al. 2005). The NE lobe might then be expected also to show a field below equipartition and a small fractional excess of X-ray emission relative to the ambient cluster, but here a field of 0.6 nT (Table 5) produces X-ray emission that exceeds our measured 90%-confidence upper limit for any X-ray excess. The measured deficit in counts as compared with cluster emission is about 13% and can be seen by eye in Figure 7. This suggests that, as in many other local radio sources (e.g., Bîrzan et al. 2004, 2008), the NE lobe has evacuated its internal X-ray emitting gas. If a lobe lying within the core radius of the cluster is evacuated of gas, then for our measured value of $\beta = 0.52$ we expect the surface brightness to be reduced by a factor that is roughly the ratio of the lobe radius ($11''$) to the core radius ($50''$), or in this case around 20%. Even allowing for plausible

Table 5. Lobe synchrotron and gas pressures

(1) Feature	(2) B_{eq} (nT)	(3) P_{eq} (10^{-12} Pa)	(4) P_{clust} (10^{-12} Pa)	(5) $B_{P_{\text{clust}}}$ (nT)
NE lobe	2.1	1.2	8.8 ± 0.4	0.6, 7.9
SW lobe	2.0	1.0	8.4 ± 0.4	0.5, 7.8

Columns (2) and (3) show equipartition magnetic field strength and pressure, respectively. Column (4) shows the cluster gas pressure at the angular distance from the core to the centre of the lobe. Column (5) gives magnetic field strengths that would result in enough synchrotron pressure to match the cluster value. Note that a 0.6 nT field in the NE lobe would violate constraints on inverse Compton X-ray emission unless there is a gas cavity at the lobe. A 0.5 nT field in the SW lobe could explain the excess X-ray seen here as inverse Compton emission (Fig. 8). Synchrotron calculations use a minimum electron Lorentz factor of $\gamma_{\text{min}} = 100$, and ignore non-uniform filling factor and protons.

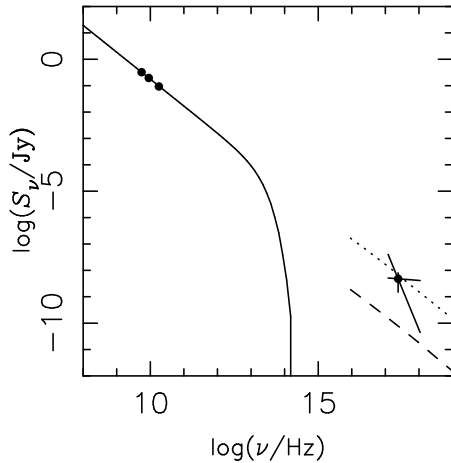


Figure 8. Radio and X-ray measurements of the SW lobe and a model of synchrotron emission (solid line) and inverse Compton scattering of the same power-law electron population on the cosmic microwave background (dotted line) and synchrotron self Compton emission (dashed line). The model is for a magnetic field strength of 0.5 nT, a factor of four below equipartition, which brings the synchrotron and external cluster pressures into agreement (Table 5).

levels of lobe inverse Compton emission, within the large uncertainties we conclude that a lobe cavity is responsible for the X-ray counts deficit.

This begs the question as to why no cavity is seen against the SW lobe. While thermal structure on scale sizes comparable to the lobes may be influencing our results (a much longer X-ray exposure would be required to map such structure), in Section 3.3 we pointed out that the NE lobe is more compact and rounded than that in SW and there is a small projected offset from the cluster centre, both suggesting motion of the radio galaxy within the potential well of the cluster towards the direction of the NE lobe. Instabilities of flow along the side of the trailing SW lobe may then have led to greater re-mixing of external gas in the SW.

We have employed the usual method of estimating the cavity power, P_{cav} of the NE lobe as $4P_{\text{clust}}V/t_s$ where

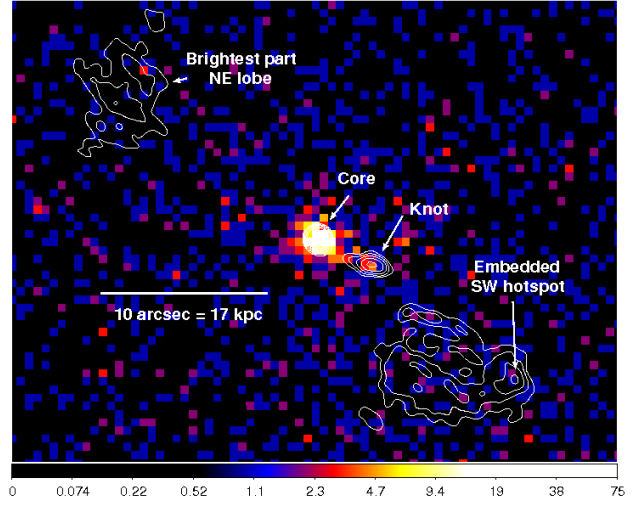


Figure 9. Contours of the 18-GHz radio map (Table 1) superimposed on unsmoothed 0.4–5 keV X-ray data in native 0.492-arcsec pixels. Colour scale is in units of counts. The contours increase by factors of 2 from the lowest level of 0.2 mJy beam $^{-1}$. Excess X-rays are seen at the core and radio knot but are not apparent in the brightest part of the NE lobe or the embedded SW hotspot.

P_{clust} is the external pressure (Table 5), V is the volume (we adopt the full 22'' lobe diameter from Table 2), and t_s is the lobe crossing time at the external sound speed (Birzan et al. 2004). Doubling the value, to account for both jets, gives a proxy for the jet power averaged over the buoyancy time of 32 Myr as $P_{\text{jet}} = 5.3 \times 10^{44}$ erg s $^{-1}$. The total 1.4-GHz radio flux density of PKS B1416–493 at 1.4 GHz is 2.6 Jy (Wright & Otrupcek 1990), giving a radio power of $P_{1.4 \text{ GHz}} = 7.3 \times 10^{41}$ erg s $^{-1}$. These measurements are within the scatter of the correlation between P_{jet} and $P_{1.4 \text{ GHz}}$ reported by (Birzan et al. 2004, 2008) and updated by Cavagnolo et al. (2010) for radio sources in cooling-flow clusters. PKS B1416–493 does not require kinetic and thermal energy of shocked gas to bring it into agreement, as is necessary for the bright well-studied southern FRI/II radio galaxy PKS B2152–699 (Worrall et al. 2012). P_{jet} is larger than the bolometric luminosity of the cluster gas out to a radius of r_{500} (Table 3), and so the jet is easily able to provide enough energy to reverse a cooling flow on the scale of the cluster core radius.

The source PKS B1416–493 then adds to the known number of cavity radio sources, and is one of a smaller group where lobe inverse Compton emission is also detected, so that lobe energetics are measured. The magnetic field is below the equipartition value, and while shocks are not detected, their presence, along with a relativistic or cold entrained proton population, cannot be excluded. The fact that like PKS B2152–699, PKS B1416–493 lies on a $P_{\text{jet}} \propto P_{\text{rad}}^{0.7}$ correlation supports the hypothesis that FRI/II boundary sources, when weighted by radio-source density, should dominate radio-galaxy heating in the local Universe. The fact that these radio sources are observed in atmospheres with a range of richness, with that of PKS B1416–493 being among the richest, means that heating is not confined to one particular type of environment.

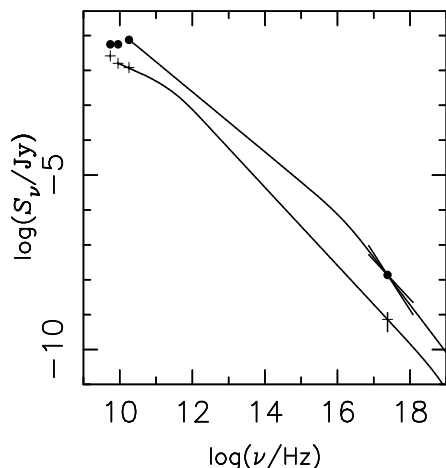


Figure 10. Radio and X-ray measurements of the core (circles) and jet knot (crosses) with possible broken-power law synchrotron spectral models. For the core $\Delta\alpha = 0.5$ is possible; inverse-Compton emission cannot be modelled because the region is unresolved and the size unknown. For the jet $\Delta\alpha > 0.5$ is needed ($\Delta\alpha = 0.7$ shown); implausibly the field would need to be almost 100 times below equipartition to give instead the jet X-rays via inverse-Compton (synchrotron self-Compton) scattering of the radio synchrotron-emitting electron population.

3.6 Core

The core of PKS B1416–493, whose X-ray counts are seen in Figure 9, has a radio spectrum that is rising at 18 GHz, indicative of self-absorption. The X-ray spectrum (containing roughly 300 counts) was measured from a circle of radius 1.25 arcsec, and was found to be well modelled with a relatively steep power law of $\alpha_x = 1.36^{+0.26}_{-0.24}$ and no excess absorption. Pileup is less than 1%, which justifies ignoring the contribution of out-of-time events from the core to the cluster emission. The 0.2–10 keV luminosity is $2.7 \times 10^{42} \text{ erg s}^{-1}$, and the flux density at 1 keV is $13.7 \pm 2.4 \text{ nJy}$. The spectral index interpolated between the radio (18 GHz) and X-ray is $\alpha_{rx} = 0.95$, typical of jet cores and knots (e.g., Balmaverde, Capetti & Grandi 2006; Harwood & Hardcastle 2012). If the X-ray is interpreted as dominated by emission from a small-scale jet and arising from the electron population responsible for the radio core, the combination of α_x and α_{rx} requires the synchrotron spectrum to steepen somewhere between the radio and X-ray, and a spectral break of $\Delta\alpha = 0.5$ is the simple prediction for energy losses (although observations of resolved jet knots often find somewhat larger breaks (e.g., Böhringer et al. 2001; Hardcastle, Birkinshaw & Worrall 2001; Birkinshaw, Worrall & Hardcastle 2002)). The data for PKS B1416–493 can be accommodated by a break at the relatively high frequency of about 10^{16} Hz if $\Delta\alpha = 0.5$ between a presumed index of $\alpha_r = 0.86$ in the radio and $\alpha_x = 1.36$ (Fig. 10). The break frequency would be lower for a larger value of $\Delta\alpha$.

The X-ray emission of PKS B1416–493’s core is thus characteristic of LERG nuclei, with the X-rays inferred to arise from the base of a jet. No excess absorption is required.

3.7 Jet knot

The radio properties of the jet knot marked in Figures 1 and 9 are given in Table 2. The X-rays have been measured from a knot-centred circle of radius 1.5 arcsec, with the cluster and other background sampled from a core-centred annulus of radii 2.06 and 5.06 arcsec, excluding the knot region. There are roughly 17 net counts. Statistical errors dominate the uncertainty in 1-keV flux density; adopting $\alpha = 1.1$ ($\Delta\alpha = 0.7$ larger than the radio spectral index, see Tab. 2 and below), we find a value of $0.75^{+0.45}_{-0.36} \text{ nJy}$.

The lower points in Figure 10 show the radio and X-ray flux densities of the knot. Given the relatively small source size, predictions for X-ray inverse-Compton radiation are dominated by the synchrotron self-Compton process, but the field strength would need to be almost 100 times below the equipartition value of 14 nT to match observations, with an implausible increase in total energy. Instead it is more likely that the X-rays are synchrotron, as inferred to be common in jet knots of FRI radio galaxies (Worrall et al. 2001), found not unusual in FRII radio galaxies (e.g., Worrall & Birkinshaw 2005; Kraft et al. 2005; Kataoka et al. 2008; Hardcastle et al. 2016), and favoured for some quasar jets (e.g., Jester et al. 2007; Cara et al. 2013; Meyer et al. 2015). The precise characteristics of the radio to X-ray spectrum cannot be determined in the absence of high-resolution observations at intermediate frequencies, but we can infer that the spectral break needs to be $\Delta\alpha > 0.5$ to accommodate the measured value of α_r and the interpolated value of α_{rx} , and $\Delta\alpha = 0.7$ is adopted in Figure 10. We also note that the registration between X-ray and radio knots is not good, with the X-rays peaking a fraction of a detector pixel upstream of the radio. This behaviour has been seen in other radio-galaxy knots for which a synchrotron origin is inferred (e.g., Hardcastle et al. 2001; Worrall & Birkinshaw 2005).

Figure 9 shows no excess X-ray emission associated with the embedded SW hotspot.

4 SUMMARY AND CONCLUSIONS

This study of PKS B1416–493 was undertaken to obtain further information on the range of gas/radio plasma interactions associated with intermediate-power radio galaxies, since such sources should be responsible for a major fraction of the radio-source heating in the Universe. PKS B1416–493 is one of the brightest such FRI/II sources, and adds to the small number of sources of this class that has been mapped with sub-kpc linear resolution in the X-ray band.

An unexpected finding of this work is that PKS B1416–493 lies within a few kpc of the centre of a hot, dense, cluster atmosphere. The host cluster has not previously been reported in optical or X-ray surveys. Radio sources of distorted shape, such as 3C 83.1B in the Perseus cluster (O’Dea & Owen 1986), are signposts to the presence of a dense gas environment, but PKS B1416–493 was known only as a relatively symmetrical double source with embedded hot spots, so only a low-mass group atmosphere was expected. PKS B1416–493 joins the roughly 30% of sources at the FRI/II boundary that are known to lie in significant groups or clusters.

The source PKS B1416–493 shows several features commonly found in deep X-ray images of intermediate-power radio galaxies. The jet displays an X-ray- and radio-bright synchrotron knot about 7 kpc from the core. The jet changes direction at this knot, and there is a significant (few hundred pc) offset between the X-ray and radio emission peaks. The NE lobe occupies a cavity in the surrounding X-ray gas, while we interpret excess counts in the SW lobe as inverse-Compton X-ray emission which, with the implied modest departure from equipartition, can bring the lobe into pressure balance with the external medium. The X-ray exposure is insufficiently deep for us to address thermal structure on the scale size of the radio source or relativistic proton content of the lobes. Only the SW lobe shows a compact hotspot, which is (as usual when only one hotspot is seen) located on the jet side of the source. The hotspot is recessed from the edge of the lobe — a feature that is sometimes interpreted as an indication of source orientation in FR II sources, but may instead be an indication of an internal disruption of the jet without significant generation of X-rays in FRI/II sources, as it is in the wide-angle tailed sources such as 3C 465 (Hardcastle et al. 2005).

We find no evidence for shocks around the lobes of PKS B1416–493. Shocks in atmospheres as hot as that around PKS B1416–493 are difficult to detect using current X-ray telescopes, and for a given input energy would be expected to exhibit a lower Mach number in a hot atmosphere than in a cool atmosphere. The clear shocks found around the similar source PKS B2152–699 (Worrall et al. 2012) would only be seen as weak temperature and X-ray surface-brightness changes if PKS B2152–699 were to be embedded in the PKS B1416–493 cluster.

The heat input from PKS B1416–493 to the cluster environment has been found to be consistent with the correlation with radio source power seen in other sources (e.g., Cavagnolo et al. 2010), and is a factor 30 higher than the power required to balance the cooling of gas within the cluster’s core radius. Such strong central heating should be driving strong convective motions in the atmosphere — the high X-ray count rate and large angular size of the cluster suggests that these motions could be detectable with the next generation of X-ray telescopes.

ACKNOWLEDGMENTS

We thank the STFC for travel support to the ATCA, and are grateful to the helpful staff at Narrabri. The scientific results reported in this article are based on observations made with the Chandra X-ray Observatory and the Australia Telescope Compact Array. The Australia Telescope is funded by the Commonwealth of Australia for operation as a National Facility managed by CSIRO. We are grateful to the Chandra X-ray Center (CXC) for its support of Chandra and the CIAO software. This research has made use of the NASA/IPAC Extragalactic Database (NED) which is operated by the Jet Propulsion Laboratory, California Institute of Technology, under contract with the National Aeronautics and Space Administration. We thank the referee for constructive comments which have helped improve the manuscript, and Leith Godfrey and Paul Nulsen for discussions of jet-power correlations.

REFERENCES

- Anders, E., Grevesse, N., 1989, *Geochimica et Cosmochimica Acta*, 53, 197
- Balmaverde, B., Capetti, A., Grandi, P., 2006, *A&A*, 451, 35
- Best, P.N., Kauffmann, G., Heckman, T.M., Ivezić, Ž., 2005, *MNRAS*, 362, 9
- Birkinshaw, M., Worrall, D.M., 1993, *ApJ*, 412, 568
- Birkinshaw, M., Worrall, D.M., Hardcastle, M.J., 2002, *MNRAS*, 335, 142
- Birzan, L., Rafferty, D.A., McNamara, B.R., Wise, M.W., Nulsen, P.E.J., 2004, *ApJ*, 607, 800
- Birzan, L., McNamara, B.R., Nulsen, P.E.J., Carilli, C.L., Wise, M.W., 2008, *ApJ*, 686, 859
- Böhringer, H. et al., 2001, *A&A*, 365, L181
- Burgess, A.M., 1998, Ph.D. Thesis, University of Sydney
- Burgess, A.M., Hunstead, R.W., 2006a, *AJ*, 131, 100
- Burgess, A.M., Hunstead, R.W., 2006b, *AJ*, 131, 114
- Cara, M. et al., 2013, *ApJ*, 773, 186
- Capetti, A., Fanti, R., Parma, P., 1995, *A&A*, 300, 643
- Cavagnolo, K.W., McNamara, B.R., Nulsen, P.E.J., Carilli, C.L., Jones, C., Birzan, L., 2010, *ApJ*, 720, 1066
- Croston, J.H., Hardcastle, M.J., Harris, D.E., Belsole, E., Birkinshaw, M., Worrall, D.M., 2005, *ApJ*, 626, 733
- Croston, J.H., Hardcastle, M.J., Mingo, B., Evans, D.A., Dicken, D., Morganti, R., Tadhunter, C.N., 2011, *ApJL*, 734, L28
- Dickey, J.M., Lockman, F.J., 1990, *ARA&A*, 28, 215
- Dunn, R.J.H., Fabian, A.C., Taylor, G.B., 2005, *MNRAS*, 364, 1343
- Fabian, A.C., 2012, *ARA&A*, 50, 455
- Godfrey, L.E.H., Shabala, S.S., 2016, *MNRAS*, 456, 1172
- Hardcastle, M.J., Birkinshaw, M., Worrall, D.M., 1998, *MNRAS*, 294, 615
- Hardcastle, M.J., Birkinshaw, M., Worrall, D.M., 2001, *MNRAS*, 326, 1499
- Hardcastle, M.J., Sakellou, I., Worrall, D.M., 2005, *MNRAS*, 359, 1007
- Hardcastle, M.J., Kraft, R.P., Worrall, D.M., Croston, J.H., Evans, D.A., Birkinshaw, M., Murray, S.S., 2007, *ApJ*, 662, 166
- Hardcastle, M.J. et al., 2012, *MNRAS*, 424, 1774
- Hardcastle, M.J. et al., 2016, *MNRAS*, 455, 3526
- Harwood, J.J., Hardcastle, M.J., 2012, *MNRAS*, 423, 1368
- Henning, J.W., Gantner, B., Burns, J.O., Hallman, E.J., 2009, *ApJ*, 697, 1597
- Hodges-Kluck, E.J., Reynolds, C.S., Cheung, C.C., Miller, M.C., 2010, *ApJ*, 710, 1205
- Ineson, J., Croston, J.H., Hardcastle, M.J., Kraft, R.P., Evans, D.A., Jarvis, M., 2015, *MNRAS*, 453, 2682
- Jester, S., Harris, D.E., Marshall, H.L., Meisenheimer, K., 2006, *ApJ*, 648, 900
- Jones, D.H. et al., 2009, *MNRAS*, 399, 683
- Kataoka J. et al., 2008, *ApJ*, 685, 839
- Kraft, R.P., Hardcastle, M.J., Worrall, D.M., Murray, S.S., 2005, *ApJ*, 622, 149
- Kraft, R.P., Azcona, J., Forman, W.R., Hardcastle, M.J., Jones, C., Murray, S.S., 2006, *ApJ*, 639, 753
- Kraft, R.P. et al., 2012, *ApJ*, 748, 19
- Mannering, E., Worrall, D.M., Birkinshaw, M., 2013, *MNRAS*, 431, 858
- McNamara, B.R., Nulsen, P.E.J., 2007, *ARA&A*, 45, 117
- McNamara, B.R., Nulsen, P.E.J., 2012, *New J. Phys.*, 14, 055023
- Meyer, E.T., Georganopoulos, M., Sparks, W.B., Godfrey, L., Lovell, J.E.J., Perlman, E., 2015, *ApJ*, 805, 154
- Nulsen, P.E.J., et al., 2013, *ApJ*, 775, 117
- O’Dea, C.P., Owen, F.N., 1986, *ApJ*, 301, 841
- O’Sullivan, E., Giacintucci, S., David, L.P., Gitti, M., Vrtillek, J.M., Raychaudhury, S., Ponman, T.J., 2011, *ApJ*, 735, 11

- Panagoulia, E.K., Fabian, A.C., Sanders, J.S., Hlavacek-Larrondo, J., 2014, MNRAS, 444, 1236
- Revnivtsev, M., Sazonov, S., Jahoda, K., Gilfanov, M., 2004, A&A, 418, 927
- Simpson, C., Ward, M., Clements, D.L., Rawlings, S., 1996, MNRAS, 281, 509
- Somerville, R.S., Davé, R., 2015, ARA&A, 53, 51
- Sun, M., 2009, ApJ, 704, 1586
- Tadhunter, C.N., Fosbury, R.A.E., Binette, L., Danziger, I.J., Robinson, A., 1987, Nature, 325, 504
- Tadhunter, C.N., Fosbury, R.A.E., di Serego Alighieri, S., Bland, J., Danziger, I.J., Goss, W.M., McAdam, W.B., Snijders, M.A.J., 1988, MNRAS, 235, 403
- Vikhlinin, A., Kratsov, A., Forman, W., Jones, C., Markevitch, M., Murray, S.S., Van Speybroeck, L. 2006, ApJ, 640, 691
- Voges, W., et al., 1999, A&A, 349, 389
- Wilson, W.E., Ferris, R.H., Axtens, P., et al., 2011, MNRAS, 416, 832
- Worrall, D.M., 2009, A&ARv, 17, 1
- Worrall, D.M., Birkinshaw, M., 1994, ApJ, 427, 134
- Worrall, D.M., Birkinshaw, M., 2005, MNRAS, 360, 926
- Worrall, D.M., Birkinshaw, M., 2006, in Alloin D., Johnson R., Lira P., eds, Lecture Notes in Physics Vol 693, Springer-Verlag, Berlin, p. 39
- Worrall, D.M., Birkinshaw, M. & Hardcastle, M.J., 2001, MNRAS, 326, L7
- Worrall D.M., Birkinshaw, M., Young, A.J., Momtahan, K., Fosbury, R.A.E., Morganti, R., Tadhunter, C.N., Verdoes Kleijn, G., 2012, MNRAS, 424, 1346
- Worrall D.M., Birkinshaw, M., Young, A.J., 2016, MNRAS, 458, 174
- Wright, A., Otrupcek, R., 1990, Parkes Radio Sources Catalogue, PKSCAT90, available on-line at <http://vizier.u-strasbg.fr>